

Cite this: *J. Mater. Chem. A*, 2020, **8**, 21265

Mechanism of enhanced ionic conductivity by rotational nitrite group in antiperovskite Na_3ONO_2 [†]

Lei Gao,^{‡abc} Hao Zhang,^{‡da} Yuechao Wang,^e Shuai Li,^{bc} Ruo Zhao,^{abc} Yonggang Wang,^{‡f} Song Cao,^a Junhua He,^{ghi} Hai-Feng Song,^e Ruqiang Zou^{‡*a} and Yusheng Zhao^{‡*bc}HPSTAR
1049-2020

Sodium-rich antiperovskite (NaRAP) ionic conductors have been considered promising inorganic electrolytes for all-solid-state sodium batteries due to their low fabrication cost, high sodium ionic conductivity and good structural tolerance. The high structural flexibility of NaRAPs allows variety of chemical substitutions to improve conductivity; in particular, the substitution of the anion cluster has effectively proved promoting Na^+ migration, both experimentally and theoretically. Herein, we report an unexpected boost in Na^+ ionic conductivity that climbs to 0.37 mS cm^{-1} at 485 K by introducing NO_2^- groups in the antiperovskite Na_3ONO_2 system. Its mechanism was fully investigated by neutron powder diffraction and DFT calculations, proving that the NO_2^- group on the lattice center, can utilize its terminal O^{2-} anion to facilitate the Na^+ migration via the Na–O interaction, when thermally excited at 485 K. The detailed migration path is also discussed by both maximum entropy method (MEM) and DFT calculations.

Received 21st July 2020
Accepted 27th September 2020

DOI: 10.1039/d0ta07110b

rsc.li/materials-a

1. Introduction

The increasing demands for large-scale energy storage systems in many fields stimulate the development of rechargeable battery technologies.^{1,2} Rechargeable sodium (Na)-ion batteries are promising candidates owing to the low cost and high abundance of sodium resources.^{3,4} Furthermore, Na-ion batteries have the advantage that many high capacity Na-cathodes do not contain cobalt, a common and high-cost

component in commercial lithium (Li)-ion cathodes.⁵ The all-solid-state Na-ion batteries employing inorganic solid electrolytes have been considered as the best choice, due to their low flammability, absence of leakage and high safety.^{6–8} Indeed, solid-state $\beta\text{-Al}_2\text{O}_3$ electrolytes have been commercialized in high-temperature sodium-sulfur (NAS) batteries,⁹ and an ionic conductivity over 1 mS cm^{-1} has been reported in NASICON-type oxide crystals at room temperature (RT).¹⁰ However, most of these electrolytes either require an elevated sintering temperature to optimize the grain-boundary resistance or have poor electrolyte–electrode contact.¹¹

Lithium-rich antiperovskite (LiRAP) superionic conductors have been considered promising solid-state electrolytes since they (a) exhibit high ionic conductivity;¹² (b) have good electrochemical stability and structural tolerance;^{13–15} (c) are compatible with lithium metal anodes;¹⁶ (d) can be processed into the desired shape and thickness at a low melting point.^{12,16,17} Meanwhile, the sodium-rich antiperovskite (NaRAP) analogues possess the same advantages as LiRAP and have also attracted increasing attention.^{18–21} Na_3OX ($\text{X} = \text{Cl}, \text{Br}, \text{and I}$) are typical NaRAP electrolytes, and the ionic conductivity of $\text{Na}_{2.9}\text{Sr}_{0.05}\text{OBr}_{0.6}\text{I}_{0.4}$ electrolytes can reach a high Na^+ conductivity of 1.89 mS cm^{-1} at 473 K through chemical manipulation.¹⁸ The isotropic three-dimensional Na^+ migration path in the NaRAP system is considered superior over other series.

To further improve the conductivity, researchers are focusing their attention to anion groups. Substituting X with a cluster (*i.e.*, $\text{Na}_3\text{S}(\text{BCl}_4)$ and $\text{Na}_3\text{O}(\text{BF}_4)$) was predicted to be an effective way to achieve higher ionic conductivity.²⁰ However,

^aBeijing Key Laboratory of Theory and Technology of Advanced Battery Material, Department of Materials Science and Engineering, College of Engineering, Peking University, Beijing 100871, China. E-mail: rzou@pku.edu.cn

^bAcademy for Advanced Interdisciplinary Studies, Department of Physics, Southern University of Science and Technology, Shenzhen 518055, China. E-mail: zhaoy@sustech.edu.cn

^cShenzhen Key Laboratory of Solid State Batteries, Guangdong Provincial Key Laboratory of Energy Materials for Electric Power, Southern University of Science and Technology, Shenzhen 518055, China

^dSchool of Metallurgical and Ecological Engineering, University of Science and Technology Beijing, Beijing 100083, China

^eLaboratory of Computational Physics, Institute of Applied Physics and Computational Mathematics, Beijing 100088, China

^fCenter for High Pressure Science and Technology Advanced Research (HPSTAR), Beijing 100094, China

^gBeijing National Laboratory for Condensed Matter Physics, Institute of Physics, Chinese Academy of Sciences, Beijing 100190, China

^hSongshan Lake Materials Laboratory, Dongguan 523808, China

ⁱSpallation Neutron Source Science Center, Dongguan 523803, China

[†] Electronic supplementary information (ESI) available. See DOI: 10.1039/d0ta07110b

[‡] These authors contributed equally to this work.

unfortunately, their experimental synthesis route is still unclear. A well-established example for Na^+ conductors in which the superhalogen cluster substitution is experimentally realized is the recently discovered Na_3OBH_4 electrolyte, which shows extremely high ionic conductivity ($\sim 4.4 \text{ mS cm}^{-1}$) even at RT due to the rotation of the BH_4^- anion group.²¹ The theoretically predicted rotational effect was finally proved by experiments, inspiring us to investigate more anion groups on the X site for faster ionic transportation.

However, only a few anion clusters can be introduced into the NaRAP lattice with careful consideration of the cluster size and strict control over the synthesis conditions (atmosphere, temperature, reagent, *etc.*). The reason that the NO_2^- anion group was specifically chosen in this work is as follows. First, the reagents Na_2O and NaNO_2 are chemically active species so that the product Na_3ONO_2 can be fabricated at a low temperature without NaNO_2 decomposition. Second, if the NO_2^- cluster can be introduced into the lattice and form the stable NaRAP structure, then it is possible to disturb the lattice in a similar way through free rotation as BH_4^- does (paddle-wheel effect). Third, the non-centrosymmetric NO_2^- group may introduce intriguing behavior to the Na^+ migration compared with the centrosymmetric BH_4^- group.

Herein, we successfully synthesized antiperovskite Na_3ONO_2 using a nitrite group (NO_2^-) as the anion cluster. From electrochemical impedance spectroscopy (EIS), its Na^+ ionic conductivity at 485 K is greatly enhanced to 0.37 mS cm^{-1} , which surpasses that of non-clustered Na_3OBr . Neutron powder diffraction refinements reveal that the thermal vibration of NO_2^- considerably increases at 485 K, coincident with the conductivity enhancement. DFT calculations demonstrate that NO_2^- rotation facilitates the Na^+ migration *via* the Na–O interaction, with a migration energy barrier as low as 0.37 eV. Therefore, we propose that the NO_2^- rotation is largely increased at 485 K in that more Na^+ cations can be pointed by and assisted by the O^{2-} (of NO_2^-) anions during migration, and hence the total ionic conductivity was improved at 485 K. This work brings to light how the acentric anion cluster affects the Na^+ migration from the perspective of ionic interaction, which provides deeper insights into improving the antiperovskite ionic conductivity using anion clusters.

2. Experimental

2.1 Synthesis

All preparations and sample treatments were performed under Ar atmosphere. Firstly, the ground Na_2O (Sigma-Aldrich, 80% (20% Na_2O_2 impurity)) and Na metal (Aladdin, 99.7%) blocks were mixed and placed in a capped alumina crucible, then heated at 523 K in a vacuum quartz tube furnace for 1 h to obtain pure Na_2O (Fig. S1†) following the reaction pathway shown in eqn (1). Experimentally, the amount of Na metal needs to be about 10% more than the Na_2O_2 impurity due to evaporation. Secondly, stoichiometric amounts of purified Na_2O and NaNO_2 (Aladdin, 99.99%) were mixed and ground with an agate mortar and pestle for 30 min, then the compound powder was pressed into 12 mm-diameter pellets under 300 MPa using

a stainless-steel die. Subsequently, the pellets were sealed in a quartz tube and heated to 583 K under vacuum at the rate of $3 \text{ }^\circ\text{C min}^{-1}$. The reaction was driven at the highest reacting temperature for 12 h following the pathway shown in eqn (2), and the products were allowed to cool naturally to room temperature in the quartz tube.



2.2 Powder X-ray diffraction and neutron powder diffraction

Powder X-ray diffraction (PXRD) measurements were conducted on a Rigaku SmartLab 9 kW diffractometer with Cu $K\alpha$ radiation ($\lambda = 1.5406 \text{ \AA}$) to identify the phases of the samples. Before measurement, each sample was sealed by Kapton film under Ar atmosphere to protect the sample from air and humidity.

Time-of-flight (TOF) neutron powder diffraction (NPD) was performed at GPPD (General Purpose Powder Diffractometer), CSNS (China Spallation Neutron Source), Dongguan Neutron Science Center. During the measurement, approximately 3 g of sample was sealed in cylindrical vanadium can, which was heated in the temperature range of 300–485 K. The data were collected using three detector banks (high-angle, 90° , and low-angle), covering a wide d -spacing from 0.05 to 28.11 \AA . The neutron flux at the sample position was at the order of $10^7 \text{ n s}^{-1} \text{ cm}^{-2}$, and the best resolution was better than 0.2% at high angle detector bank.²²

2.3 Differential scanning calorimetry

Differential scanning calorimetry (DSC) analysis was conducted on a Setaram DSC 131 instrument, and samples were sealed in an aluminum crucible under N_2 atmosphere with a heating and cooling rate of $5 \text{ }^\circ\text{C min}^{-1}$ from 323 to 623 K.

2.4 Electrochemical impedance spectroscopy

Ionic conductivities were measured by electrochemical impedance spectroscopy (EIS) in the temperature range of 380–513 K, using an electrochemical work station analyzer (Zennium, Zahner) at frequencies ranging from 1 Hz to 1 MHz with an amplitude of 50 mV. Na_3ONO_2 powders were hot-pressed into pellets (diameter = 10 mm, thickness $\sim 1.2 \text{ mm}$) under 300 MPa in an insulative die with an annealing temperature of 373 K for 5 h, and two stainless-steel rods (diameter = 10 mm) were clamped on both sides of the sample as current collectors. During the EIS measurement, the die with gaskets was hermetic enough to protect the sample from air and humidity.

2.5 Rietveld Refinements and maximum entropy method analysis

Rietveld Refinements on TOF NPD under different temperatures were performed by the Fullprof suite software.²³ The crystal lattice parameters, ion locations, and anisotropic thermal displacements were carefully refined, clearly

demonstrating the lattice expansion and higher ion vibrations as the temperature increased. Maximum Entropy Methods (MEM) were performed based on the refined structure factors.

The MEM analysis was used to reveal possible sodium ion migration pathways. The structure factors and standard uncertainties obtained by refinements were analysed by MEM with Dysnomia.²⁴ The unit cells of antiperovskites were divided into $300 \times 300 \times 300$ voxels. The detailed method for MEM analysis can be found in ref. 25.

2.6 First-principles calculation

In the present computational work, Kohn–Sham density-functional theory with the projector-augmented wave (PAW) method^{26,27} implemented in the Vienna Ab-initio Simulation Package (VASP)^{28,29} was used. The Climbing Image Nudged Elastic Band (CI-NEB) as implemented in the Transition State Tools for VASP (VTST) package^{30,31} was used for the calculation of transition states and barriers. The PBEsol GGA^{32,33} was used in all calculations. For all structural optimization and CI-NEB calculations, the plane-wave cutoff energy was set to be 400 eV, and Γ -centered $6 \times 6 \times 6$ k -meshes were used for the primitive unit cell of Na_3OBr and Na_3ONO_2 . For the $2 \times 2 \times 1$ supercell for calculating the migration of Na, a $3 \times 3 \times 6$ k -mesh was used. Noteworthily, the lattice parameters used in the CI-NEB calculation were based on the values obtained by Rietveld refinements according to the NPD data at the corresponding experimental temperature, and the supercell volume was fixed during calculations.

3. Results

3.1 Phase analysis

Fig. 1(a) is the PXRD pattern of Na_3ONO_2 at room temperature. All peaks are assigned to the cubic NaRAP-type Na_3ONO_2 phase ($Pm\bar{3}m$) without any other distinct impurities. Inspired by the synthesis route of Na_3ONO_2 , we also investigated the possible synthesis of NaRAP-type Na_3ONO_3 with the triangular NO_3^- group *via* solid-state reactions between Na_2O and NaNO_3 . To our surprise, the product is an orthorhombic Na_3NO_4 phase with a tetrahedral NO_4^{3-} group rather than antiperovskite phase (Fig. S2†).³⁴ The reason can be referred to the fact that the Goldschmidt tolerance factor $t \sim 1.08$ of Na_3ONO_3 is out of the stable range from 0.8 to 1.0 (eqn (3)) for a stable perovskite structure,^{35,36} where R_{Na} is the radius of Na^+ (0.95 Å), R_{O} is the radius of O^{2-} (1.40 Å) and R_{X} is the radius of NO_3^- (2.64 Å).^{20,37} Noteworthily, during the synthesis of Na_3ONO_2 , poor vacuum conditions will cause the reagent NaNO_2 to partially oxidize to NaNO_3 that leads to a small amount of Na_3NO_4 impurity in the final product (Fig. S2†). Therefore, the vacuum conditions need to be carefully prepared to avoid impurities.

One of the merits of antiperovskites is their low melting point feature that enables easy fabrication. The thermal stability and melting point of Na_3ONO_2 were analyzed by DSC.^{18,21} The endothermic and exothermic peaks represent the melting and crystallization temperature of the sample, respectively. As shown in Fig. 1(b), the melting point of Na_3ONO_2 is about 536 K,

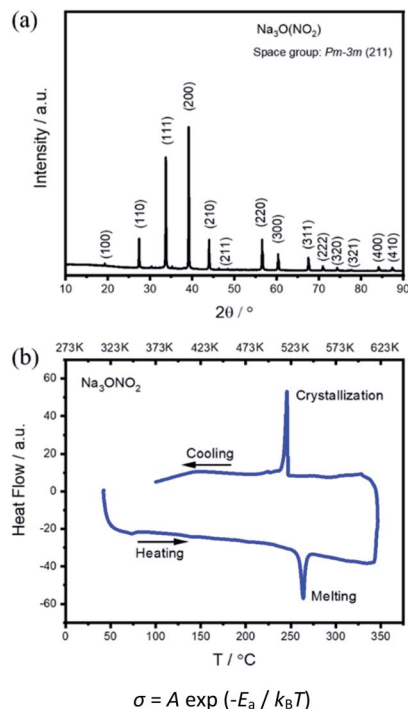


Fig. 1 (a) Powder XRD pattern of synthesized Na_3ONO_2 is indexed in space group $Pm\bar{3}m$ with assigned Miller indices. (b) Differential scanning calorimetry (DSC) curve of synthesized Na_3ONO_2 .

which is higher than that of Na_3OBr and Na_3OBH_4 .^{18,21} The discontinuous NO_2^- order–disorder transition temperature is 178 K, which is out of our temperature scanning range.³⁸ Except for the melting/crystallization peaks, no other abnormal endothermic and exothermic peaks appeared in our DSC results. The melting peak is higher than that reported in early work,³⁹ and the peak related to increased NO_2^- mobility is not observed. In contrast, isomorphous $\text{Na}_3\text{OBr}_{0.5}\text{I}_{0.5}$ needs a higher temperature of 499 K to reach Br^-/I^- disorder,¹⁸ demonstrating that NO_2^- thermal vibrations are more sensitive to temperature.

$$t = (R_{\text{Na}} + R_{\text{X}}) / \sqrt{2}(R_{\text{Na}} + R_{\text{O}}) \quad (3)$$

3.2 Ionic conductivity

The ionic transport properties of Na_3ONO_2 were analyzed by temperature-dependent EIS. The Nyquist curves reflect the current response of Na_3ONO_2 electrolyte at different frequencies and temperatures under a voltage disturbance (Fig. 2(a)). Taking the Nyquist curve at 395 K as a representative, as shown in Fig. 2(b), it exhibits a typical semicircle (in fact two superimposed semicircles) at high frequency representing the bulk and grain boundary resistance in series, and one Warburg-type region at low frequency representing ion blocking electrode. These are characteristics of a pure ionic conductor. Fitting this plot at 395 K by the equivalent circuit leads to a total resistance of 389.1 kΩ, including the bulk resistance R_1 of 29.1 kΩ and the grain boundary resistance R_2 of 360 kΩ. The grain boundary resistance R_2 is one order of magnitude higher than the bulk

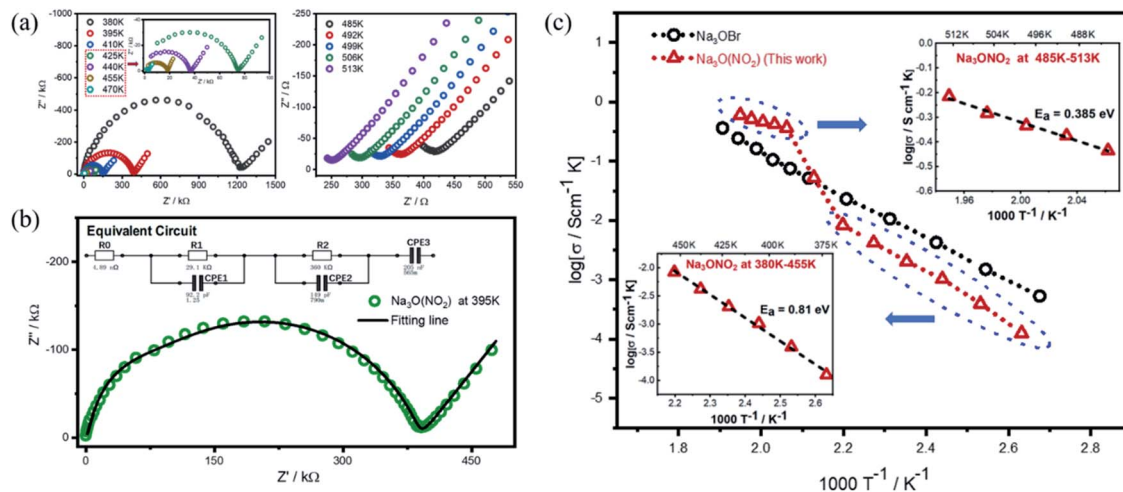


Fig. 2 (a) Nyquist curves of Na_3ONO_2 in the temperature range from 380 to 513 K. (b) Fitting curve with the equivalent circuit for Nyquist plot of Na_3ONO_2 at 395 K. (c) Arrhenius conductivity plot of Na_3ONO_2 in the temperature range from 380 to 513 K, the conductivity data of Na_3OBr are reproduced from the work of Wang *et al.*¹⁸

resistance R_1 , demonstrating the fact that oxide electrolytes usually have high grain boundary resistance.

Fig. 2(c) is the Arrhenius plot illustrating the relationship between Na^+ conductivity and temperature in the range from 380 K to 513 K. The Na^+ conductivity in reported Na_3OBr is used for comparison.¹⁸ In contrast to the Na_3OBr , of which the ionic conductivity steadily increases in the whole range, the ionic conductivity of Na_3ONO_2 at first stays lower below 455 K, then suddenly jumps to 0.37 mS cm^{-1} at 485 K that even surpasses the reported Na_3OBr .¹⁸ This unexpected sharp increase renders the Na_3ONO_2 superior to Na_3OBr in the range from 485 to 513 K. Noteworthy, this measurement is reversible (Fig. S3 and S4[†]), and the sharp increase occurs before the melting peak ($\sim 536 \text{ K}$), so it should be related somehow to an intrinsic behaviour and does not result from melting behaviour. The insets in Fig. 2(c) present two distinct activation energies, $E_a \sim 0.81 \text{ eV}$ from 380 to 455 K and $E_a \sim 0.385 \text{ eV}$ from 485 to 513 K, obtained from the slope in the Arrhenius plots based on eqn (4), where σ is the conductivity, A is the pre-exponential parameter, E_a is the activation energy, T is absolute temperature and k_B is the Boltzmann constant.

$$\sigma = A \exp(-E_a/k_B T) \quad (4)$$

3.3 Structural determination

The unexpected enhancement of the Na^+ ionic conductivity from 410 to 485 K should be ascribed to the NO_2^- group. Firstly, we explain from the perspective of the crystal structure. The neutron powder diffraction measurements were performed at selected temperatures before and after the enhancement to identify structural changes, as shown in Fig. 3(a). All peaks can be simulated by the Rietveld refinement and the schematic crystal structure with anisotropic thermal displacements is provided in Fig. 3(b). In the cubic lattice (Fig. 3(b) and S5[†]), the O anions at the vertex (0, 0, 0) serve as the center of the Na_6O

octahedra, and these octahedra are corner-linked *via* Na cations in the middle of the lattice edges (0.5, 0, 0). Each cubic lattice only has one NO_2^- group around the lattice center, but has 6 and 24 crystallographically equivalent positions for each N and O anion, respectively. The occupation is therefore 1/6 for each N position and 2/24 for each O position. The structural model adopted here is a disordered one, which could be further discerned as six different orientations of the NO_2^- group by NMR.³⁸ The anisotropic thermal displacements are also shown here as ellipsoids (Fig. 3(b)), and we notice that Na mainly vibrates along the vertical plane of the lattice edge. Detailed information on the refinement results and parameters are provided in Tables 1 and S1.[†] The most significant change is the thermal displacements of Na^+ and the NO_2^- group. In Fig. 3(c), their anisotropic displacement parameters *versus* temperature are plotted. From room temperature to 410 K, their displacements rise gradually. But from 410 to 485 K, all the Na^+ , N^{3+} , and O^{2-} undergo a sudden increase in their anisotropic displacements. In the NO_2^- group, the N^{3+} axial parameter (U_{11}) jumps from 0.0217 at 410 K to 0.0540 at 485 K, indicating that the thermal vibration becomes stronger along the axial direction. In the meantime, its bonding O^{2-} also exhibits much higher thermal displacements, with all three parameters (U_{11} , U_{22} , U_{33}) increasing. Apparently, the thermal vibration of the NO_2^- group grows much stronger from 410 to 485 K. For Na^+ , its axial (U_{11} , towards the octahedral center) and equatorial displacements ($U_{22} = U_{33}$) all exhibit considerable increases after 410 K. The most intriguing thing is that this sudden increase in Na_3ONO_2 does not appear in Na_3OBr , of which the Na^+ thermal displacements (U_{11} , U_{22} , U_{33}) seem to reach saturation from 410 K to 485 K. Considering the fact that the conductivity is also enhanced in this range, the sudden increase of Na^+ and NO_2^- displacements should correlate with the Na^+ conductivity enhancement. In Fig. 3(d), the lattice parameter of Na_3ONO_2 keeps expanding all the way. One may argue that this lattice thermal expansion can also be the explanation for the

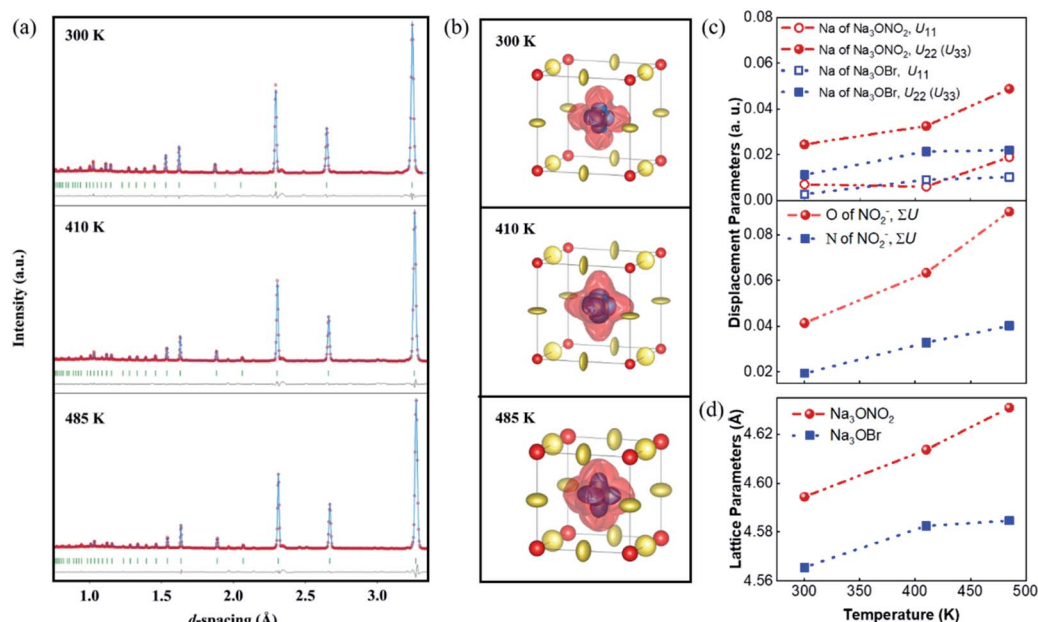


Fig. 3 (a) Rietveld refinement of Na_3ONO_2 based on NPD at 300 K, 410 K and 485 K. (b) Schematic crystal structure of Na_3ONO_2 at 300 K, 410 K and 485 K with anisotropic thermal displacements. Yellow sphere represents Na, red represents O, and blue represents N. (c) Displacement parameters of Na atoms in Na_3ONO_2 and displacement parameters of N and O atoms in the NO_2^- group as a function of temperature in the range 300–485 K. (d) Lattice parameters of Na_3ONO_2 and Na_3OBr as a function of temperature in the range 300–485 K.

enhancement, since larger space is usually beneficial for Na^+ migration. However, we notice that the parameter of Na_3ONO_2 grows more steadily, in sharp contrast to the U of O (NO_2^-). If lattice expansion is the reason, then the ionic conductivity should exhibit a steady increase rather than a boost. Hence, it is highly possible that the significantly intensified thermal vibration of NO_2^- at high temperature promotes the Na^+ migration, while isotropic Br^- in Na_3OBr has no such effect.

Maximum Entropy Method (MEM) calculations were performed based on the neutron diffraction data at 485 K. The (100), (020), (001) planes were specifically provided to show the nuclear density around the Na^+ ions at the plane intersection (Fig. 4(a)). From the (100) plane distribution (Fig. 4(b)), it is readily observed that Na^+ ions transport among the nearest-neighbouring Na^+ sites along the edges within the Na_6O octahedron, as indicated by the arrow. The Na^+ ions move close to the central O^{2-} before migrating to the neighboring Na^+ position. Compared with Na_3OBr (Fig. S6†), the nuclear density distributions along the lattice edges are more obvious, which is consistent with the Na^+ conductivity enhancement facilitated by stronger NO_2^- group vibration.

DFT calculations were performed to reveal how the NO_2^- group affects Na^+ migration. As shown in Fig. 5, at the start (I), a Na^+ vacancy (yellow circle) was introduced on the corner between two adjacent Na_6O octahedra. This decreases the electron density around O^{2-} of NO_2^- , so its O^{2-} has to get closer to the migrating Na^+ to compensate for its electron density. After structural optimization, the O^{2-} would always point toward the migrating Na^+ . The whole process (I–VI) involves Na^+ /vacancy migration (yellow arrow), NO_2^- group rotation (red arrow), and corresponding structure adjustments. Here, the Na^+ migration energy barrier is considered the key factor in determining the ionic conductivity. The distance (grey dashes) variation between migrating Na^+ and O^{2-} is also scrutinized to help understand the whole process. Finally, the energy barrier at 485 K in this model is calculated to be 0.37 eV, which is about 0.05 eV lower than the 0.42 eV of Na_3OBr , indicating that the migration activity is higher, which is consistent with the above conductivity measurements.

The NO_2^- group directly participates in the migration process in a rotational way, with its O^{2-} anion (red arrow) pointing towards the migrating Na^+ cation. In the beginning,

Table 1 Refined Crystal Parameters Based on NPD for Na_3ONO_2 at 300, 410, and 485 K

Formula	Lattice params (\AA)	Thermal params (Na)			Thermal params (N)	Thermal params (O of NO_2^-)
		U_{11}	U_{22}	U_{33}	ΣU	ΣU
Na_3ONO_2	$a = 4.594(4)$ at 300 K	0.007	0.025	0.025	0.01933	0.04133
	$a = 4.616(6)$ at 410 K	0.006	0.033	0.033	0.03283	0.06333
	$a = 4.630(9)$ at 485 K	0.019	0.049	0.049	0.0402	0.09017

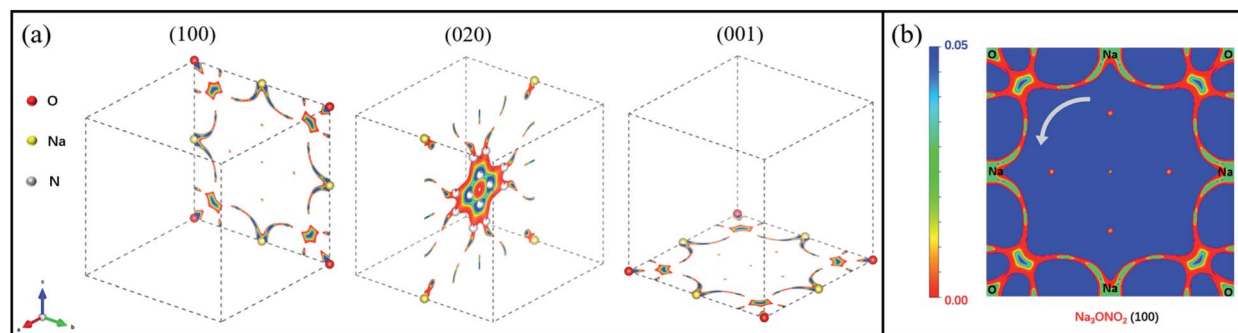


Fig. 4 The nuclei density distributions of Na_3ONO_2 deduced from MEM analysis based on NPD at 485 K: (a) (100) (020) (001) planes. The NO_2^- density distribution around the lattice center is also shown in the (020) plane. (b) The detailed two-dimensional contour maps sliced on the (100) plane. The arrow represents the Na^+ migration path.

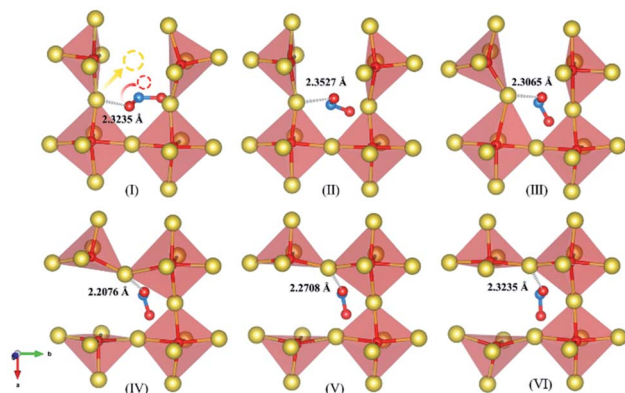


Fig. 5 Detailed information on the migration process at 485 K. We extracted several calculation steps from the whole process, including the beginning (I) stage, four intermediate stages (II–V), and the final stage (VI). Yellow spheres represent Na and red spheres represent O. The yellow arrow and red arrow represent the Na^+ migration and NO_2^- rotation. The yellow circle is the Na vacancy, and also the final position for the migrating Na^+ . The red circle is the final position for the O^{2-} of NO_2^- .

the rotary NO_2^- tries to drive its O^{2-} a little bit away from the migrating Na^+ , with the distance increasing from the original 2.3235 to 2.3527 Å. After that, the Na^+ gradually moves to the vacancy position with the help of the NO_2^- group, as seen in stages (III and IV) of Fig. 5. The distance between Na^+ and O^{2-} can be as low as 2.2076 Å in the intermediate step (IV), but soon climbs to 2.2708 Å as the Na^+ approaches the final position. In the final stage (VI), the NO_2^- group further rotates clockwise, and the Na_6O coordination framework makes further adjustments, with the Na–O distance recovering to 2.3235 Å. Throughout the process, the O^{2-} of NO_2^- assists the Na^+ migration by pulling it into the intermediate position, then pushing it away to the final position. From these results, we propose that the rotary NO_2^- group can facilitate Na^+ migration *via* the interaction between its O^{2-} anion and Na^+ cation.

We notice that only this type of migration can lead to an energy barrier as low as 0.37 eV, which results in the superior conductivity of Na_3ONO_2 . In another set of models where the NO_2^- group is fixed (not allowed to move or rotate in the whole process, Fig. S7†), the Na^+ migration energy barrier climbs up to

1.37 eV. Also, if we place some restraints on the NO_2^- group (Fig. S7†), that is, keeping its N–O bond nearly vertical to the x – y plane around the migrating Na^+ so that the group rotation would be limited, the energy barrier increased to 0.79 eV. These comparative results further confirm the positive effects of NO_2^- free rotation. If the group is fixed or restrained, their pointed Na^+ ions will suffer from a much higher energy barrier and the migration is slowed down.

The last comparative study we examined is the migration behaviour of specific Na^+ ions away from NO_2^- (not pointed by its terminal O^{2-}), since this is also possible in a real situation. This part is carefully discussed in the ESI (Fig. S8 and S9†). In this case, the lattice exhibits a higher energy in both the initial and transitional states, which means a metastable pathway is possible. Moreover, although sent away at the beginning, the Na^+ will be re-pointed by another NO_2^- from the neighbouring lattice in the final stage, since the energy can be lower in this instance. Generally, this type of migration may not be energy favored, but still reflects the fact that when O^{2-} points to Na^+ , it can stabilize the lattice.

Based on the above analysis, it is not difficult to explain the experimental results. Below 410 K, the NO_2^- thermal vibration or rotation is not high enough to promote more Na^+ migration. The NO_2^- group in one lattice has a certain orientation and hence the number of Na^+ that can be assisted (or pointed) by the O^{2-} of NO_2^- is actually limited. Those Na^+ without the help of NO_2^- can also migrate but their paths are not that efficient. However, the situation changes as the temperature increases. Above 485 K, as revealed by neutron diffraction data, the NO_2^- thermal vibration significantly increased, indicating that the NO_2^- rotation is much stronger. Therefore, more Na^+ cations have opportunities to be pointed by O^{2-} of NO_2^- and are assisted by Na–O interaction so that the Na^+ conductivity of Na_3ONO_2 surpasses that of Na_3OBr .

4. Discussion

4.1 Channel size

The migrating ion size and available free space in the lattice are two intuitive factors. Usually, the ionic conductivity of inorganic solid-state electrolytes can be optimized by enlarging the

Table 2 Calculated Channel Size (CS) of Na₃OBr²⁰ and Na₃ONO₂. Where LP, V_{Na} , V_{A} , V_{O} are lattice parameter, volume of Na⁺, volume of Br⁻ (NO₂⁻), and volume of O⁻, respectively

Crystal	LP (Å)	V_{Na} (Å ³)	V_{A} (Å ³)	V_{O} (Å ³)	CS (Å ³)	V_{Na}/CS
Na ₃ OBr	4.565	6.53	25.24	8.37	61.52	0.106
Na ₃ ONO ₂	4.594	6.53	32.7	8.37	55.88	0.117

volume of the unit cell, which facilitates the ion diffusion in the transport channel.^{17,40} However, both the migrating ion size and the free space for transport need to be taken into account.^{20,41} Therefore, the ratio of the migrating ion size (volume V_{Na}) to the channel size (CS) as a descriptor is more convincing than simply the cell volume itself. Here the CS is obtained by subtracting the N and O ion volume (except for Na⁺) from the cell volume.²⁰ As shown in Table 2, according to the structural information obtained from Rietveld refinement at RT, the lattice parameter (4.594 Å) of Na₃ONO₂ is larger than that of Na₃OBr (4.565 Å), but the CS (55.88 Å³) of Na₃ONO₂ is smaller than that of Na₃OBr (61.52 Å³). Since the migrating ion size is the same ($V_{\text{Na}} \sim 6.53$ Å³), there is a smaller free space for Na⁺ transport in the crystal lattice of Na₃ONO₂. Hence, the lower ionic conductivity of Na₃ONO₂ than that of Na₃OBr may be attributed to the smaller channel size in the low temperature range of 380 to 455 K.

4.2 Rotation of NO₂⁻

However, the conductivity enhancement from 455 to 485 K needs to be carefully discussed. First, for most inorganic crystalline solid-state electrolytes, the ionic conductivity can be enhanced by the phase transition.^{16,42–48} The Li₂OHCl conductivity was remarkably improved after the phase transition from orthorhombic to cubic around 303–323 K.¹⁶ Similarly, there are significant differences in the ionic conductivity and activation energy between tetragonal and metastable cubic Li₇La₃Zr₂O₁₂.^{17,40,42} However, according to the refinement of Na₃ONO₂ (Table 1), there is no strong evidence corresponding to an observable structural phase transition (whether continuous or discontinuous) above 300 K. The space group remains cubic $Pm\bar{3}m$ throughout the whole temperature range from 300 to 485 K. Second, introducing Li⁺/Na⁺ defects is a common strategy in promoting ion migration.^{49–51} This strategy was not adopted here in our experiment. From refinements, the Na ions are almost fully occupied (0.95–1) in both Na₃ONO₂ and Na₃OBr. So, lattice defects should not be responsible for the conductivity improvement around 485 K.

The mechanism of the conductivity enhancement is the intensified rotational effect of the NO₂⁻ group around 455–485 K. Below 455 K, the NO₂⁻ is disordered with rapid rotation, but its thermal vibration/rotation is not yet strong enough to fully promote the Na⁺ migration and only a few Na⁺ ions can be facilitated by Na–O (of NO₂⁻) interaction. At this time, the channel size effect is predominant. Compared to Na₃OBr, the lower channel size in Na₃ONO₂ accounts for its lower conductivity. When the temperature rises to 485 K, NO₂⁻ is thermally stimulated to a more intensive rotational state so that more Na⁺ can be facilitated *via* Na–O (of NO₂⁻) interactions and the conductivity is therefore

boosted. Meanwhile, the activation energy reduced from 0.81 eV to 0.385 eV according to the Arrhenius plot and the energy barrier is reduced to 0.37 eV (lower than Na₃OBr at 0.42 eV) according to the DFT calculation, respectively. The comparative calculation studies also support the above statement. If the rotation is restrained or totally fixed, the energy barrier would rise to 0.79 eV or 1.37 eV, respectively, indicating that the stronger free rotation is needed to boost the conductivity. More studies on the NO₂⁻ rotation barrier are provided in the ESI (Fig. S11†).

5. Conclusion

In conclusion, Na₃ONO₂ was successfully synthesized by a low temperature solid-state reaction. ESI measurements show a superior ionic conductivity in Na₃ONO₂ (0.37 mS cm⁻¹, $E_{\text{a}} \sim 0.385$ eV) around 485 K. Neutron powder diffraction refinements and DFT calculations reveal the mechanism of the conductivity enhancement. Above 485 K, the NO₂⁻ rotation is more intensified than that at lower temperature, which can significantly facilitate Na⁺ ion migration *via* Na–O interactions. The Na₃ONO₂ migration energy barrier is calculated to be 0.37 eV lower than that of Na₃OBr (0.42 eV) with the NO₂⁻ rotation, which is consistent with the experimental results. This work gives a detailed explanation of how the anion cluster affects the Na⁺ migration behavior, which provides more insight into designing superionic antiperovskite electrolytes.

Author contributions

Zou, R. and Zhao, Y. conceived the idea; Gao, L. and Zhang, H. designed the experiments with the guidance of Zou, R. and Zhao, Y.; Gao, L. performed the XRD, DSC and electrochemical measurements with assistance from Li, S., Zhao, R. and Gao, S.; Gao, L. performed the NPD measurements with the assistance from He, L. and Li, S.; Zhang, H. performed the Rietveld refinement and MEM analysis with the assistance from Gao, L. and Wang, Y.; Wang, Y. performed the DFT calculation with the guidance of Song, H.; Gao, L. and Zhang, H. prepared this manuscript with assistance from all other co-authors.

Conflicts of interest

There are no conflicts to declare.

Acknowledgements

This work was financially supported by the National Natural Science Foundation of China (51825201), Key Program of the National Natural Science Foundation of China (51732005), National Science Foundation of China (51902150), Guangdong Provincial Key Laboratory of Energy Materials for Electric Power (2018B030322001), Shenzhen Key Laboratory of Solid State Batteries (ZDSYS20180208184346531), the Science Challenge Project (No. TZ2016004 and No. TZ2018002), the National Key Research and Development Program of China (2017YFA0206701), National Program for Support of Top-Notch Young Professionals, and Changjiang Scholar Program.

References

- 1 D. Larcher and J. M. Tarascon, *Nat. Chem.*, 2015, **7**, 19–29.
- 2 J. W. Choi and D. Aurbach, *Nat. Rev. Mater.*, 2016, **1**, 16013.
- 3 N. Yabuuchi, K. Kubota, M. Dahbi and S. Komaba, *Chem. Rev.*, 2014, **114**, 11636–11682.
- 4 W. Zhou, Y. Li, S. Xin and J. B. Goodenough, *ACS Cent. Sci.*, 2017, **3**, 52–57.
- 5 W. D. Richards, T. Tsujimura, L. J. Miara, Y. Wang, J. C. Kim, S. P. Ong, I. Uechi, N. Suzuki and G. Ceder, *Nat. Commun.*, 2016, **7**, 11009.
- 6 S. Wenzel, T. Leichtweiss, D. A. Weber, J. Sann, W. G. Zeier and J. Janek, *ACS Appl. Mater. Interfaces*, 2016, **8**, 28216–28224.
- 7 J. Y. Hwang, S. T. Myung and Y. K. Sun, *Chem. Soc. Rev.*, 2017, **46**, 3529–3614.
- 8 A. Hayashi, K. Noi, A. Sakuda and M. Tatsumisago, *Nat. Commun.*, 2012, **3**, 856.
- 9 K. B. Hueso, M. Armand and T. Rojo, *Energy Environ. Sci.*, 2013, **6**, 734–749.
- 10 Q. Ma, M. Guin, S. Naqash, C.-L. Tsai, F. Tietz and O. Guillon, *Chem. Mater.*, 2016, **28**, 4821–4828.
- 11 Z. Zhang, Q. Zhang, J. Shi, Y. S. Chu, X. Yu, K. Xu, M. Ge, H. Yan, W. Li, L. Gu, Y.-S. Hu, H. Li, X.-Q. Yang, L. Chen and X. Huang, *Adv. Energy Mater.*, 2017, **7**, 1601196.
- 12 Y. Zhao and L. L. Daemen, *J. Am. Chem. Soc.*, 2012, **134**, 15042–15047.
- 13 A. Emly, E. Kioupakis and A. Van der Ven, *Chem. Mater.*, 2013, **25**, 4663–4670.
- 14 S. Li, J. Zhu, Y. Wang, J. W. Howard, X. Lü, Y. Li, R. S. Kumar, L. Wang, L. L. Daemen and Y. Zhao, *Solid State Ionics*, 2016, **284**, 14–19.
- 15 X. Lu, G. Wu, J. W. Howard, A. Chen, Y. Zhao, L. L. Daemen and Q. Jia, *Chem. Commun.*, 2014, **50**, 11520–11522.
- 16 Z. D. Hood, H. Wang, A. Samuthira Pandian, J. K. Keum and C. Liang, *J. Am. Chem. Soc.*, 2016, **138**, 1768–1771.
- 17 T. Famprakis, P. Canepa, J. A. Dawson, M. S. Islam and C. Masquelier, *Nat. Mater.*, 2019, **18**, 1278–1291.
- 18 Y. Wang, Q. Wang, Z. Liu, Z. Zhou, S. Li, J. Zhu, R. Zou, Y. Wang, J. Lin and Y. Zhao, *J. Power Sources*, 2015, **293**, 735–740.
- 19 J. Zhu, Y. Wang, S. Li, J. W. Howard, J. Neufeind, Y. Ren, H. Wang, C. Liang, W. Yang, R. Zou, C. Jin and Y. Zhao, *Inorg. Chem.*, 2016, **55**, 5993–5998.
- 20 H. Fang and P. Jena, *ACS Appl. Mater. Interfaces*, 2019, **11**, 963–972.
- 21 Y. Sun, Y. Wang, X. Liang, Y. Xia, L. Peng, H. Jia, H. Li, L. Bai, J. Feng, H. Jiang and J. Xie, *J. Am. Chem. Soc.*, 2019, **141**, 5640–5644.
- 22 J. Chen, L. Kang, H. Lu, P. Luo, F. Wang and L. He, *Phys. B*, 2018, **551**, 370–372.
- 23 J. Rodríguez-Carvajal, Recent developments of the program FULLPROF, *Commission on Powder Diffraction (IUCr) Newsletter*, 2001, vol. 26, pp. 12–19.
- 24 K. Momma, T. Ikeda, A. A. Belik and F. Izumi, *Powder Diffr.*, 2013, **28**, 184–193.
- 25 F. Izumi and K. Momma, *IOP Conf. Ser.: Mater. Sci. Eng.*, 2011, **18**, 022001.
- 26 P. E. Blochl, *Phys. Rev. B: Condens. Matter Mater. Phys.*, 1994, **50**, 17953–17979.
- 27 G. Kresse and D. Joubert, *Phys. Rev. B*, 1999, **59**, 1758–1775.
- 28 G. Kresse and J. Furthmüller, *Comput. Mater. Sci.*, 1996, **6**, 15–50.
- 29 G. Kresse and J. Furthmüller, *Phys. Rev. B*, 1996, **54**, 11169–11186.
- 30 G. Henkelman, B. P. Uberuaga and H. Jónsson, *J. Chem. Phys.*, 2000, **113**, 9901–9904.
- 31 G. Henkelman and H. Jónsson, *J. Chem. Phys.*, 2000, **113**, 9978–9985.
- 32 J. P. Perdew, K. Burke and M. Ernzerhof, *Phys. Rev. Lett.*, 1996, **77**, 3865–3868.
- 33 G. I. Csonka, J. P. Perdew, A. Ruzsinszky, P. H. T. Philipsen, S. Lebègue, J. Paier, O. A. Vydrov and J. G. Ángyán, *Phys. Rev. B*, 2009, **79**, 155107.
- 34 M. Jansen, *Angew. Chem., Int. Ed.*, 1977, **16**, 534–535.
- 35 Z. Wang, H. Xu, M. Xuan and G. Shao, *J. Mater. Chem. A*, 2018, **6**, 73–83.
- 36 Z. Li, M. Yang, J.-S. Park, S.-H. Wei, J. J. Berry and K. Zhu, *Chem. Mater.*, 2015, **28**, 284–292.
- 37 E. R. Nightingale, *J. Phys. Chem.*, 1958, **63**, 1381–1387.
- 38 G. Klösters, L. van Wüllen and M. Jansen, *Phys. Chem. Chem. Phys.*, 2002, **4**, 3461–3466.
- 39 M. Jansen, *Angew. Chem., Int. Ed. Engl.*, 1991, **30**, 1547–1558.
- 40 J. C. Bachman, S. Muy, A. Grimaud, H. H. Chang, N. Pour, S. F. Lux, O. Paschos, F. Maglia, S. Lupart, P. Lamp, L. Giordano and Y. Shao-Horn, *Chem. Rev.*, 2016, **116**, 140–162.
- 41 H. Fang and P. Jena, *Proc. Natl. Acad. Sci. U. S. A.*, 2017, **114**, 11046–11051.
- 42 C. A. Geiger, E. Alekseev, B. Lazic, M. Fisch, T. Armbruster, R. Langner, M. Fechtelkord, N. Kim, T. Pettke and W. Weppner, *Inorg. Chem.*, 2011, **50**, 1089–1097.
- 43 K. Meier, T. Laino and A. Curioni, *J. Phys. Chem. C*, 2014, **118**, 6668–6679.
- 44 G. Schwering, A. Hönnerscheid, L. van Wüllen and M. Jansen, *ChemPhysChem*, 2003, **4**, 343–348.
- 45 Y. Harada, T. Ishigaki, H. Kawai and J. Kuwano, *Solid State Ionics*, 1998, **108**, 407–413.
- 46 Y. Harada, Y. Hirakoso, H. Kawai and J. Kuwano, *Solid State Ionics*, 1999, **121**, 245–251.
- 47 Z. Liu, W. Fu, E. A. Payzant, X. Yu, Z. Wu, N. J. Dudney, J. Kiggans, K. Hong, A. J. Rondinone and C. Liang, *J. Am. Chem. Soc.*, 2013, **135**, 975–978.
- 48 M. Tachez, J.-P. Malugani, R. Mercier and G. Robert, *Solid State Ionics*, 1984, **14**, 181–185.
- 49 K. Oh, D. Chang, B. Lee, D.-H. Kim, G. Yoon, I. Park, B. Kim and K. Kang, *Chem. Mater.*, 2018, **30**, 4995–5004.
- 50 X. Zhan, S. Lai, M. P. Gobet, S. G. Greenbaum and M. Shirpour, *Phys. Chem. Chem. Phys.*, 2018, **20**, 1447–1459.
- 51 T. Fuchs, S. P. Culver, P. Till and W. G. Zeier, *ACS Energy Lett.*, 2019, 146–151, DOI: 10.1021/acsenerylett.9b02537.